Research Article | Vol. 29, No. 14 / 5 July 2021 / Optics Express 22315
Optics EXPRESS

Fourier transform spectrometer based on high-repetition-rate mid-infrared supercontinuum sources for trace gas detection

M. A. Abbas,[1] K. E. Jahromi,[1] M. Nematollahi,[1] R. Krebbers,[1] N. Liu,[1,2] G. Woyessa,[3] O. Bang,[3,4,5] L. Huot,[5] F. J. M. Harren,[1] and A. Khodabakhsh[1,*]

[1]*Trace Gas Research Group, Department of Molecular and Laser Physics, Institute for Molecules and Materials, Radboud University, 6525 AJ Nijmegen, The Netherlands*
[2]*Laser Spectroscopy and Sensing Laboratory, School of Physics and Materials Science, Anhui University, 230601 Hefei, China*
[3]*DTU Fotonik, Department of Photonics Engineering, Technical University of Denmark, DK-2800 Kgs. Lyngby, Denmark*
[4]*NORBLIS IVS, Virumgade 35D, 2830 Virum, Denmark*
[5]*NKT Photonics, Blokken 84, 3460 Birkerød, Denmark*
[*]*a.khodabakhsh@science.ru.nl*

Abstract: We present a fast-scanning Fourier transform spectrometer (FTS) in combination with high-repetition-rate mid-infrared supercontinuum sources, covering a wavelength range of 2–10.5 μm. We demonstrate the performance of the spectrometer for trace gas detection and compare various detection methods: baseband detection with a single photodetector, baseband balanced detection, and synchronous demodulation at the repetition rate of the supercontinuum source. The FTS uses off-the-shelf optical components and provides a minimum spectral resolution of 750 MHz. It achieves a noise equivalent absorption sensitivity of $\sim 10^{-6}$ cm^{-1} Hz$^{-1/2}$ per spectral element, by using a 31.2 m multipass absorption cell.

1. Introduction

Fourier transform spectroscopy is a widely used and a well-established method. For decades, it has been the golden standard for chemical detection and characterization of solid, liquid and gas-phase samples. It can provide a broad spectral bandwidth and high spectral resolution, especially in the mid-infrared (MIR) molecular fingerprint region. However, it is traditionally provided with incoherent thermal light sources, which are omnidirectional and have low spectral brightness. Therefore, achieving a long interaction length in gas-phase samples is quite a challenge. In addition, long averaging times are needed to obtain a spectrum with a high resolution and high signal-to-noise ratio (SNR).

Newly developed ultra-broadband MIR supercontinuum (SC) light sources show a strong potential to replace the thermal light sources in Fourier Transform Spectrometers (FTSs). SC sources are spatially coherent and have the potential to cover a wider spectral wavelength range than thermal sources. They provide a very high spectral brightness, much higher than thermal sources and even exceeding the brilliance of a synchrotron [1–5]. Furthermore, they have the potential to deliver ultra-flat broadband spectra [6], which is highly desirable for Fourier transform spectroscopy to achieve a uniform detection sensitivity over their spectral coverage. Historically, the main drawback of SC sources has been their high Relative Intensity Noise (RIN), due to noise amplification in the nonlinear broadening process [7,8]. Recently, low-noise near-infrared (NIR) SC sources have been demonstrated using all-normal dispersion photonic crystal fibers [9] and recent advancements in cascading-based MIR SC sources provide reduced RIN noise, due to

#425995 https://doi.org/10.1364/OE.425995
Journal © 2021 Received 25 Mar 2021; revised 12 May 2021; accepted 14 May 2021; published 30 Jun 2021

Optics EXPRESS

gain-induced soliton alignment in the in-amplifier SC used as a seed [10]. The technology of MIR SC sources with sub-nanosecond pulse durations and MHz repetition rates has now become sufficiently mature to be used in various applications, such as Optical Coherence Tomography (OCT), spectroscopy, and microscopy [11–14]. The MHz repetition rate can be utilized in synchronous demodulation, to overcome the 1/f noise in the system [15]. In combination with an FTS, the high repetition rate yields a fast demodulation process in the detection system, allowing the FTS to keep a fast scanning speed.

Over the past decade, mechanical FTSs in combination with MIR Optical Frequency Comb (OFC) sources (which are both spatially and temporally coherent) have also shown great improvements in the best achievable detection sensitivity, measurement time, spectral coverage and spectral resolution [16–20]. However, direct broadband MIR OFC sources, covering instantaneously the MIR molecular fingerprint region, are not available yet. Presently, broadband MIR OFC generation is based on nonlinear frequency conversion of NIR OFC sources, employing Difference Frequency Generation (DFG) [21] or Optical Parametric Oscillation (OPO) [22]. Direct MIR OFCs based on Quantum Cascade Lasers (QCLs) and Interband Cascade Lasers (ICLs) demonstrate a promising potential, especially in dual-comb spectroscopy [23,24], however their instantaneous spectral coverage is still quite limited. Despite the superior performance of the nonlinear-conversion-based MIR OFC sources combined with FTSs, their complexity of operation, instantaneous wavelength coverage, and price prevents users to consider them as a better substitute for incoherent sources.

The advancements in NIR/MIR SC sources make them a viable alternative to replace incoherent sources in commercial FTS systems, especially for gas-phase applications [25]. This transition seems inevitable, considering the foreseen improvements in the properties of MIR SC sources: ultra-flat broadband spectra, high spectral brightness, low RIN, low price, and small size [2]. Recently, the combination of high-repetition-rate NIR/MIR SC sources with commercial FTS devices has been demonstrated utilizing various detection systems; such as synchronous demodulation [26], photoacoustics [27], and lock-in amplification [28]. However, the commercial FTSs are optimized for use with thermal light sources and usually require some modifications and adjustments to operate properly with pulsed SC sources [12,28].

Here we present a cost-effective, home-built FTS, using only off-the-shelf optical components, especially developed to work with ultra-broadband and high-repetition-rate MIR SC sources. The FTS operates in the 1–12 μm wavelength region (due to the employed photodetectors it is limited to 2–11 μm), with a minimum spectral resolution of 750 MHz, which is adequate for pressure-broadened gas-phase spectroscopy. To evaluate the performance of the developed FTS for trace gas detection, we employed a multipass cell (MPC) to increase the light-matter interaction path length. Note that, high-finesse resonance cavities can provide much longer effective interaction lengths compared to MPCs. However, high-finesse cavities only have a long effective path length in a limited wavelength range, due to the limited high-reflection bandwidth of the mirror coatings. This considerably restricts the useful wavelength coverage of the spectrometer for high sensitive detection. The high optical power of the novel MIR SC sources makes it possible to employ MPCs with long interaction path lengths and still measure an interferogram with high SNR.

Here, we present the first demonstration of trace gas detection with a long-wavelength MIR SC source whose spectrum extends beyond 5 μm. We demonstrate the performance of the system for three different cases: (I) using a single photodetector operating in the baseband, (II) using synchronous demodulation of the photodetector output referenced to the SC repetition rate, and (III) utilizing a balanced detection scheme in the baseband. Note that the overall performance of a similar spectrometer based on a short-wavelength MIR supercontinuum source, using a balanced detection scheme in the baseband has been already shown in our previous work [29]. Here, we focus on the technical details of the developed spectrometer, e.g. optical layout and

Optics EXPRESS

signal processing, as well as the comparison of different detection systems. We also demonstrate and study the performance of the spectrometer using a long-wavelength MIR supercontinuum source.

2. Experimental setup and procedures

The experimental setup is illustrated in Fig. 1(a), including a top view of the FTS. Two different SC sources were used with the developed FTS. The first SC source is commercially available from NKT Photonics (SuperK MIR). It has a repetition rate of 2.5 MHz, a spectral coverage of 1.4–4.1 µm, and a total average power of ~450 mW. The second SC source has been developed by DTU Fotonik. It is based on an Erbium:Ytterbium (Er:Yb) master oscillator power amplifier (MOPA) followed by a cascade of different fibers comprising pieces of Thulium (Tm) doped, ZBLAN, Arsenic trisulfide (As_2S_3), and Arsenic triselenide (As_2Se_3) fibers [30]. This SC source has a spectral coverage of 1.5–10.5 µm, a total average power of ~86 mW, a pulse duration of ~0.5 ns, and a repetition rate of 3.0 MHz. In both cases, the SC beam (depicted in green) is transmitted through a Herriott MPC (HC30L, Thorlabs) with a nominal optical path length of 31.2 m, which contains the gas sample. The MPC is connected to a gas handling system, including flow/pressure controllers, capable of changing the gas flow in the range of 0 to 50 lh^{-1} and the pressure from 5 mbar to 1 bar.

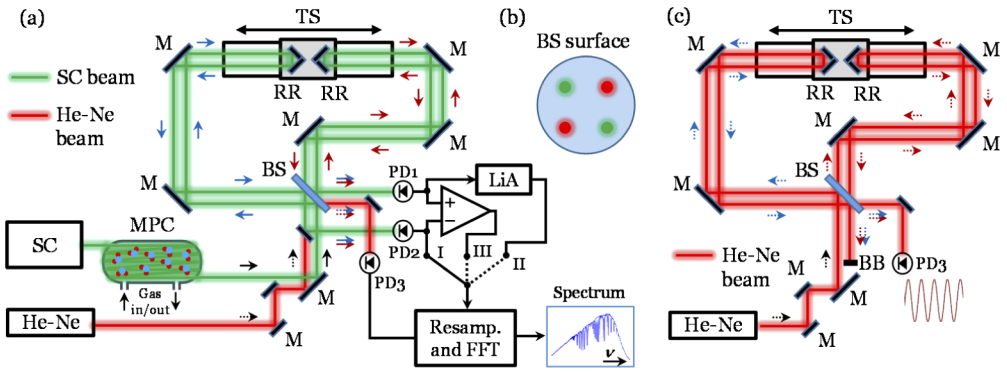

Fig. 1. (a) The experimental setup (top view of the FTS). SC: supercontinuum source, He-Ne: Helium-Neon laser, MPC: multipass cell, M: mirror, BS: beamsplitter, RR: retroreflector, TS: translation stage, LiA: lock-in amplifier. (b) The beam pattern on the surface of the beamsplitter. The two bottom beams are the insertion beams and the two top beams are the reflected beams from the retroreflectors. (c) The propagation pattern of the He-Ne laser beam in the FTS. BB: beam blocker.

The output beam of the MPC is sent to the FTS, which is based on a Michelson interferometer. The beamsplitter (BS, BSW711, Thorlabs) in the FTS splits the insertion beam into the two arms. In each arm, the SC beam is directed towards a hollow retroreflector mirror (RR, HRR201-P01, Thorlabs), using MIR enhanced protected gold mirrors (M, PF10-03-M02, Thorlabs). The propagation direction of the SC beam is shown in Fig. 1(a) using red arrows for the right arm and blue arrows for the left arm of the Michelson interferometer. The two retroreflectors are used back-to-back in the two arms to reflect the SC beam parallel to the insertion beam, but with a horizontal and vertical offset. To clarify this, Fig. 1(b) demonstrates the position of the SC beams on the surface of the beam splitter. The bottom right green spot is the insertion beam and the top left green spot is the superposition of the reflected beams from the retroreflectors of the two arms. Therefore, the reflected SC beams from the two arms are recombined on the beam splitter and construct two pairs of beams transmitted through and reflected from the beamsplitter. Each pair is sent to a thermoelectrically cooled MCT photodetector to record the

Optics EXPRESS

two (out-of-phase) interference patterns. We used PVI-4TE-4 photovoltaic detectors (Detectivity 2.0×10^{11} cm.Hz$^{1/2}$/W, Cut-off frequency 5 MHz, Vigo Systems) for the shorter wavelength SC source (from NKT Photonics), and PVI-4TE-10.6 photovoltaic detectors (Detectivity 4.5×10^{9} cm.Hz$^{1/2}$/W, Cut-off frequency 5 MHz, Vigo Systems) for the longer wavelength SC source (from DTU Fotonik). The rest of the components in the spectrometer were the same for the two SC sources.

The two back-to-back retroreflectors are mounted on a 10 cm linear-motor translation stage (TS, DDSM100, Thorlabs), thus the optical path difference (OPD) in the FTS is four times the physical travelling distance of the translation stage. By precise positioning of the mirrors after the beam splitter, the zero OPD of the FTS is adjusted to the center of the translation stage. Therefore, for a full 10 cm scan range of the translation stage, the maximum OPD of the FTS is 40 cm (OPD = ±20 cm), which can provide a spectral resolution of $1/40 = 0.025$ cm^{-1} or 750 MHz. Note that the spectral resolution is defined by the spacing of the consecutive points in the spectrum and no apodization function was utilized. By scanning the translation stage, the interference pattern (interferogram) of each pair of SC beams is recorded by the corresponding photodetector (PD_1 and PD_2). To demonstrate the performance of the MIR SC-based FTS, we record the interferogram in three different detection schemes: (I) directly from one of the photodetectors in the baseband, (II) by demodulating the output of one of the photodetectors using a fast digital lock-in amplifier (Moku:Lab, Liquid Instruments) referenced to the repetition rate of the SC source, and (III) using balanced detection in the baseband and removing the common intensity noise by a differential amplifier (SR560, Stanford Research Systems) in the output of the two photodetectors. The result of each scheme is digitized by an analog-to-digital converter (ADC, NI 6251, National Instruments) and sent to a LabVIEW program developed for signal processing, data visualization, and recording.

The OPD of the FTS needs to be calibrated before performing a Fourier transformation on the SC interferogram. The calibration is performed by recording the interference pattern from a Helium-Neon (He-Ne, HNL050LB, Thorlabs) laser, whose beam (depicted in red) is propagating in parallel with the SC beam in the FTS. For clarity, the propagation direction of the He-Ne laser beam is shown in Fig. 1(c) using red dash-arrows for the right arm and blue dash-arrows for the left arm of the Michelson interferometer. The positions of the He-Ne laser beams on the surface of the beam splitter are illustrated in Fig. 1(b). The bottom left red spot is the insertion beam and the top right red spot is the superposition of the reflected beams from the retroreflectors of the two arms. The reflected He-Ne laser beams from the two arms are recombined on the beam splitter, and construct two pairs of beams transmitted through and reflected from the beamsplitter. One pair of beams is directed to a Si amplified photodetector (PD_3, PDA8A2, Thorlabs) to record the interference pattern of the He-Ne laser beam; the other pair is dumped on a beam-blocker (BB). The obtained interferogram of the He-Ne laser beam is digitized by the ADC and sent to the LabVIEW program for OPD calibration of the SC interferogram.

The linear-motor translation stage can be operated up to 500 mm/s velocity; however, in different detection schemes, two distinct parameters limit the maximum velocity of the translation stage in practice. In single-detector and balanced detection schemes (I and III), the limiting factor is the maximum sample rate of the analog-to-digital converter (ADC). In order to properly detect the interferogram of the He-Ne laser beam that is suitable for OPD calibration, at least four data-points are needed per period of the interference pattern. Therefore, the maximum sample rate of the ADC sets the speed limit on the linear stage to ensure that four points per period can be recorded. Since the maximum detected frequency in the interferogram of the MIR SC is at least ~4 times lower than the He-Ne interferogram, no further precautions are needed for the SC interferogram, concerning the velocity of the translation stage. For recording the two interferograms simultaneously, the maximum sampling frequency of the ADC is 0.6 MS/s which

Optics EXPRESS

renders a maximum velocity of 20 mm/s for the translation stage. By choosing a fast ADC, this additional constraint would be removed.

Using the lock-in detection scheme (II) forces another limit to the velocity of the translation stage, which is the time constant (inverse of the filter bandwidth) of the lock-in amplifier. Generally, a trade-off between the SNR and the measurement time exists for any lock-in detection. In this implementation of the lock-in amplification with the FTS, the time constant of the lock-in amplifier should be much shorter (e.g. by ~10 times) than the shortest period in the MIR SC interferogram. In other words, the filter bandwidth of the lock-in amplifier should be broad enough (i.e. the time constant should be adequately short), to keep the measured SC interferogram undistorted. Empirically, we found that a lock-in time constant of ~80 µs (i.e. averaging 200 to 260 pulses of the shorter/longer-wavelength SC sources) would yield a residual intensity modulation lower than the total detection noise level. Therefore, by considering an 80 µs time constant and dictating the shortest period in the MIR SC interferogram to be much higher than this time, a maximum velocity of ~20 mm/s for the translation stage is obtained in the case of the lock-in detection scheme. Note that in the lock-in detection scheme, in addition to the maximum sampling frequency of the ADC, a second limiting factor is the repetition rate of the SC source, since a lower repetition rate requires a longer time constant to achieve a similar residual intensity modulation, rendering a lower maximum velocity of the translation stage. One can alternatively lock-in to higher harmonics of the repetition rate of the SC source; however, higher harmonics will render a weaker modulated signal to start with. In addition, a broader electrical bandwidth in the detection system will be needed, which increases the total detection noise. We chose a maximum velocity of 20 mm/s for the lock-in detection, since it also matches the maximum velocity in the baseband detection schemes and simplifies the comparisons for detection sensitivity.

3. Calibration of the optical path difference

In all of the different detection schemes, both interferograms of the SC and the He-Ne laser are recorded by the ADC. The ADC is internally clocked and its data sampling is asynchronous with respect to the He-Ne laser interferogram. In a real-time data processing routine, we first remove the DC offset of the two interferograms, then use a linear interpolation to find the exact positions of the zero crossings in the quasi-sinusoidal interferogram of the He-Ne laser. Finally, we find the intensities of the SC interferogram at these particular positions by another linear interpolation on the SC interferogram. The entire process can be seen as a resampling of the SC interferogram at the zero crossing positions of the He-Ne interferogram. Therefore, the OPD in the SC interferogram is calibrated up to the wavelength stability of the He-Ne laser, and independent of the velocity fluctuations of the translation stage. By pre-measuring the wavelength of the He-Ne laser, the OPD step size is a well-known parameter. Therefore, Fourier transformation of the OPD-calibrated SC interferogram yields the MIR spectrum in terms of a calibrated wavenumber domain. More sophisticated OPD calibration and signal processing routines for FTS combined with an SC source can be found in literature [31], which provide much better precision and accuracy needed for low-pressure gas-phase precision spectroscopy. Our current signal processing routine provides a sufficient precision for our application of trace gas detection at atmospheric pressure, without introducing unnecessary complications.

To clarify the OPD calibration routine, Fig. 2 demonstrates the performance of the calibration process on two simulated sine waves, representing the He-Ne laser interferogram (star markers in blue) and the MIR SC interferogram (cross markers in red), after removing the DC offset. The two simulated interferograms experience a frequency decrease (exaggerated for clarity) to mimic a velocity drop in the mechanical stage of the FTS. The algorithm finds the zero-crossings of the He-Ne laser interferogram (circular markers in green) by linear interpolation. Then, it linearly interpolates the SC interferogram (circular markers in black) at the zero-crossing

Optics EXPRESS

positions of the He-Ne laser interferogram. Now considering the interpolated SC interferogram in the zero-crossing domain, it is calibrated with an optical path difference step size equal to the zero-crossing intervals.

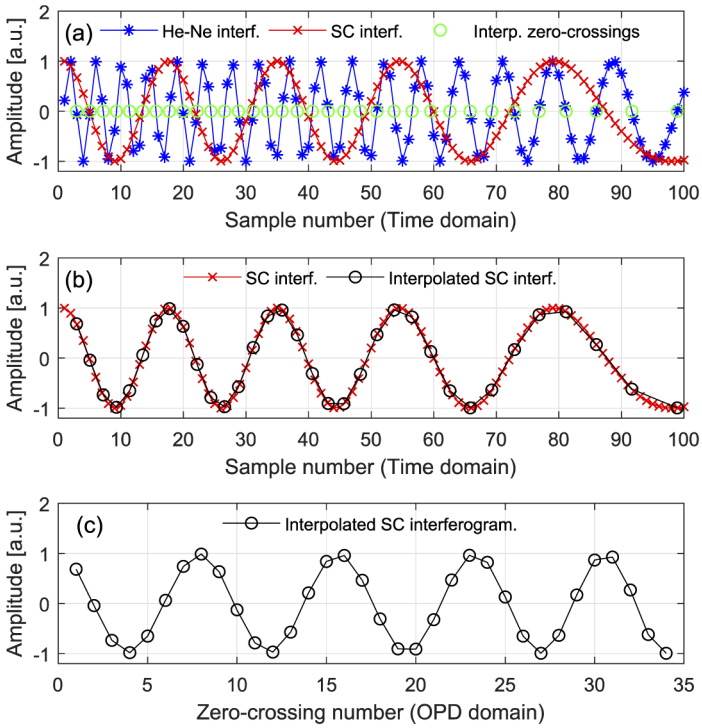

Fig. 2. A demonstration of the optical path difference calibration routine applied to two simulated sine waves with changing frequency, representing the He-Ne laser and MIR SC interferograms. (a) The simulated He-Ne laser interferogram (star markers in blue) and the SC interferogram (cross markers in red), both experiencing a frequency decrease modeling a velocity drop in the mechanical stage of the FTS, along with the zero-crossing points of the He-Ne interferogram (circular markers in green) calculated by linear interpolation. All of the curves are in the sample number (time) domain. (b) The simulated SC interferogram (cross markers in red) along with the (linearly) interpolated SC interferogram (circular markers in black) at the zero-crossing positions of the He-Ne interferogram in the sample number (time) domain. (c) The same interpolated SC interferogram at the zero-crossing positions of the He-Ne interferogram (circular markers in black) in the zero-crossing (calibrated OPD) domain. The regular periodicity in the OPD domain, demonstrates the cancellation of velocity fluctuations of the linear stage.

A more conventional OPD calibration method can be performed by synchronizing the data acquisition of the MIR SC interferogram to the zero crossings of the He-Ne interference. In other words, the ADC might be externally and directly clocked by the zero crossings of the He-Ne interferogram. Considering the fluctuations in the velocity of the translation stage and also the acceleration/deceleration process close to the two ends of the stage (in case these spans are considered in the data acquisition), an ADC with a high dynamic range of direct external clock frequency would be needed. In addition, by recording the He-Ne interferogram and performing the OPD calibration in the signal processing routine, it is possible to resample the MIR SC interferogram at any interpolated intervals between the zero crossings of the He-Ne interferogram. This is especially useful if the reference cw laser is changed from a He-Ne laser to a more compact

Optics EXPRESS

and stable cw NIR laser, or when a short-wavelength spectral coverage in the visible range is needed. In this case, one can further interpolate between the zero crossings of the reference laser interferogram to achieve a desirable OPD step size with respect to the shortest wavelength in the measured spectrum. Note that using an ADC with an internal clock and a data acquisition process triggered by an external event is not a proper choice. The reason is the variable (and usually not well-known) latency between the zero crossings of the He-Ne interferogram (external trigger) and the next internal clock cycle of ADC, in which the MIR SC interferogram is sampled. This variable latency degrades the precision of the OPD calibration yielding less precise and even distorted MIR spectra.

4. Results

We measured the intensity spectrum of the short- and long-wavelength SC sources, using the developed FTS, with a spectral resolution of 8 GHz. The results are shown in Fig. 3. The visible absorption lines, especially apparent in the spectrum of the long-wavelength SC source, are due to the presence of atmospheric water vapor in the beam path from the SC source to the detector(s) of the FTS. Therefore, it is crucial to purge the beam-path in the FTS spectrometer with Nitrogen to minimize the spectral interference by water absorption lines onto the measured spectra, while using the long-wavelength SC source. Note that the wavelength coverage for both SC sources is slightly wider than the demonstrated spectra in Fig. 3. For the short-wavelength SC source, we used a Germanium window (WG91050-C9, Thorlabs) in the beam path, with ~2 μm cut-on wavelength, to prevent the photodetector(s) from saturation due to the residual pump power. For the long-wavelength SC source, the limiting factor is the cut-off wavelength of the utilized photodetectors. The actual spectral coverage is 1.4–4.1 μm for the short-wavelength source and 1.5–10.5 μm for the long-wavelength source, as mentioned earlier.

Although most of the spectral power lies in the 3.4–4.0 μm region for the short-wavelength source and the 5.0–7.9 μm region for the long-wavelength source, it is possible to perform spectroscopy in the other wavelength ranges with high SNR values, thanks to the high average power of the SC sources and the sensitive photodetectors. Using optical bandpass filters, one can select a desired wavelength range, covering the absorption spectrum of a specific gas or combination of gases, and block undesired wavelength ranges from reaching the photodetector(s). This is a common practice used with FT-IR spectrometers, which prevents intensity saturation of the photodetector by an undesired part of the MIR spectrum and, as a result, provides a spectrum with a higher SNR for the desired wavelength range.

4.1. Short-wavelength supercontinuum source

To compare the performance of different detection schemes, we used the short-wavelength SC source (from NKT Photonics) and measured the spectrum of a gas mixture containing 25.0(7) ppm of Ethyl acetate ($C_4H_8O_2$) and 5.0(1) ppm of Ethane (C_2H_6), diluted in N_2 at atmospheric pressure. This gas mixture was produced from two calibrated gas bottles of 100 ppm Ethane in N_2 and 100 ppm Ethyl acetate in N_2 both further diluted in pure N_2, using three mass flow controllers (EL-FLOW Prestige FG-201CV, Bronkhorst) with mass flows of 5 lh^{-1} for Ethyl acetate, 1 lh^{-1} for Ethane, and 14 lh^{-1} for N_2. The gas mixture was connected to the inlet of the MPC and the total pressure in the MPC was set at atmospheric pressure using a pressure controller (EL-PRESS P-702CV, Bronkhorst) and a vacuum pump connected in series in the outlet of the MPC. We also measured the background spectrum in pure N_2 at atmospheric pressure and normalized the transmission spectrum of the sample gas to the background spectra. The absorbance (αL) spectrum of the sample was calculated by applying a natural logarithm to the normalized spectrum. We used an optical bandpass filter (FB3250-500, Thorlabs, 500 nm transmission band centered at 3.25 μm) in the beam path after the MPC to limit the spectrum to the absorption band of the gases. The measurement results using the three aforementioned

Optics EXPRESS

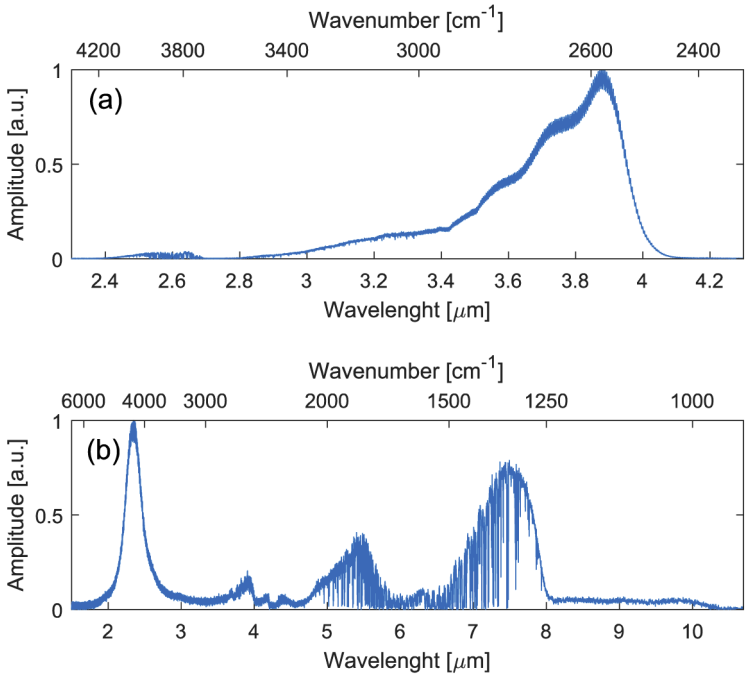

Fig. 3. The spectra (in linear intensity scale) of (a) the short-wavelength SC source and (b) the long-wavelength SC source with spectral resolution of 8 GHz. The absorption lines in the two spectra are due to the atmospheric water vapor present in the beam path from the SC source to the detector(s) of the FTS.

detection methods are shown in Fig. 4. The measured spectra (3 GHz spectral resolution, 500 averages in ~15 minutes) are shown in black. We used the PNNL database [32] for calculating the model spectra of Ethyl acetate (in blue, inverted) and Ethane (in red, inverted) and the combined model spectra (in green, inverted). In addition to the model spectra, we used a 3rd order polynomial in the fitting routine to remove the slowly varying baseline from the measured spectra. The fitting routine is based on a standard least square method with the concentration of different species as the fitting parameters [16]. The retrieved concentrations from the fit for the three detection methods are 24(2) ppmv Ethyl acetate and 5.2(8) ppmv Ethane using a single detector in baseband (detection method I) shown in Fig. 4(a), 25.3(7) ppmv Ethyl acetate and 4.9(3) ppmv Ethane using a single detector and a lock-in amplifier (detection method II) shown in Fig. 4(b), and 25.6(3) ppmv Ethyl acetate and 4.8(1) ppmv Ethane using balanced detection (detection method III) shown in Fig. 4(c). The error values are the standard deviation of the concentrations retrieved from ten consecutive measurements.

The standard deviations of the noise in the featureless part of the residuals are $\sigma_I = 0.091$ for the baseband single-detector detection scheme, $\sigma_{II} = 0.035$ for the synchronous detection scheme, and $\sigma_{III} = 0.0068$ for the balanced detection scheme. Therefore, the SNR values of the synchronous and balanced detection schemes are ~2.6 and ~13 times better than the SNR of the baseband single-detector detection scheme, respectively. This comparison shows that, although synchronous detection (referenced to the repetition rate of the SC source using a lock-in amplifier) can increase the SNR in the spectrum, the best result is achieved from a baseband balanced detection.

Using a lock-in amplifier can reduce the 1/f noise by performing the detection at a higher frequency, as already shown in [28] for liquid-phase spectroscopy. However, the main component

Optics EXPRESS

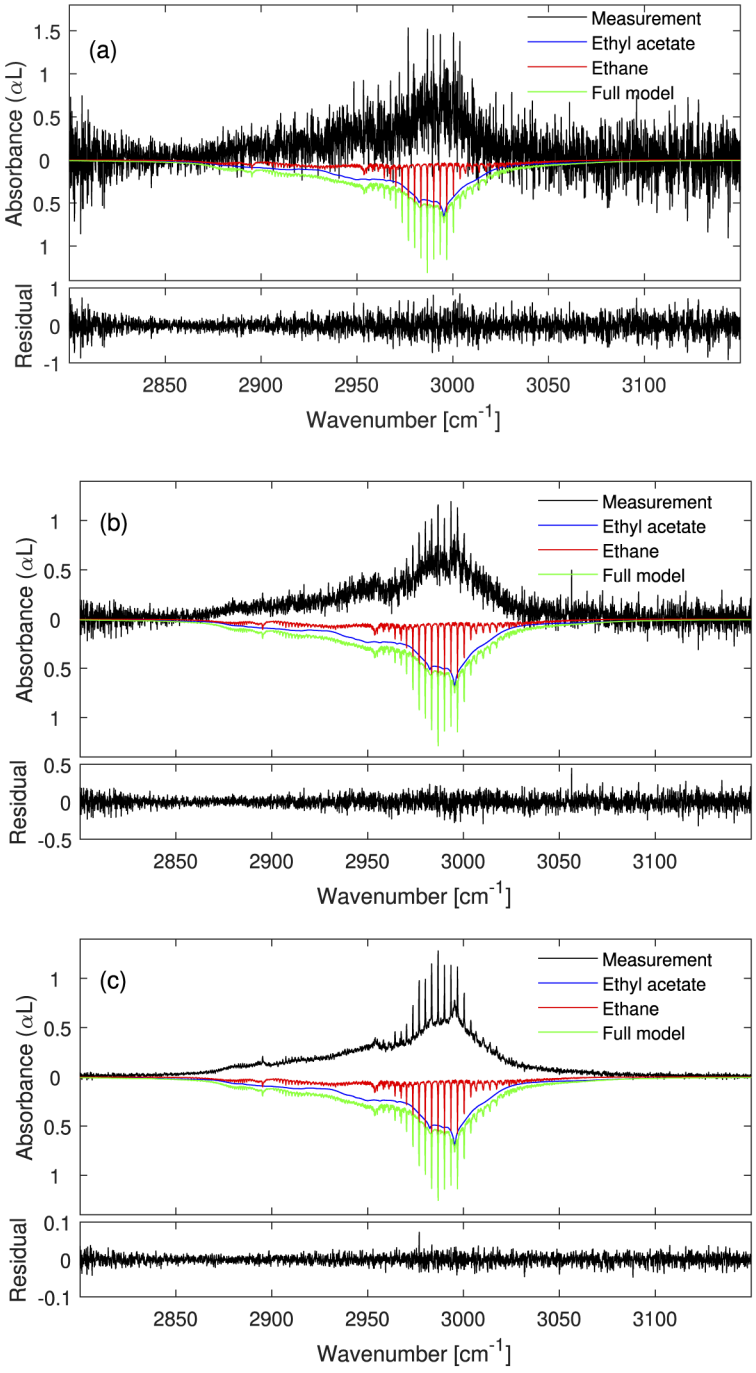

Fig. 4. Measured spectra (in black, 3 GHz spectral resolution, 500 averages in ~15 minutes) and fitted model spectra for a mixture of 5 ppmv of Ethane (in red, inverted) and 25 ppmv of Ethyl acetate (in blue, inverted), both diluted in N_2 at atmospheric pressure for three different detection methods: (a) single detector in baseband, (b) synchronous detection using a lock-in amplifier, and (c) balanced detection. Model spectra are calculated using PNNL database and the combined model spectra are shown in green and inverted for clarity.

Optics EXPRESS

of the SC noise is its pulse-to-pulse fluctuation. This fluctuation is directly mapped to the down-converted signal of the lock-in amplifier, limiting the noise reduction factor of this method. Note that synchronous detection accompanied with a balancing method [26] yields a much higher SNR improvement, compared to synchronous detection using a single photodetector. Therefore, a large portion of noise reduction can be attributed to the balanced detection method.

In balanced detection, the two interferograms received by the detectors are out-of-phase. However, the intensity noise of the SC source is common on both of the detectors. By subtracting the output voltage of the two detectors, the out-of-phase interferograms are added together, while the common-mode noise on the two signals is effectively subtracted from each other. Therefore, the SNR of the subtracted signal is improved drastically compared to the single detector scheme, and it also has a better efficiency compared to the synchronous detection. The enhancement factor of the balanced detection is highly dependent on the balancing quality of the two out-of-phase interferograms before the subtraction (in the electrical domain), considering both the amplitude and phase of the two electrical signals.

Since the best results are achieved using the balanced detection scheme, we used this detection method for the measurements presented in the rest of this article. For all presented spectra, the same spectral normalization method and fitting routine are used, as well as considering a 3rd order polynomial to remove the baseline. For the gas species available in the HITRAN database [33], we used this database (and a Voigt profile) to simulate the absorption model spectra for the fits. For the species not available in the HITRAN database, we use the PNNL database [32] for modeling. All measurements are performed at room temperature.

To evaluate the performance of the instrument at high spectral resolution, we measured the spectrum of 5.0(1) ppmv of CH_4 diluted in N_2 at 900 mbar total pressure, with 1 GHz spectral resolution around 3.2 μm, using the same optical bandpass filter (FB3250-500, Thorlabs) in the NKT SC beam path. The measured spectrum is demonstrated in Fig. 5 (in black, 250 averages in ~25 minutes) alongside a fitted model of CH_4 spectrum (in blue, inverted for clarity). The model spectrum is calculated using the HITRAN database parameters and a Voigt profile. The retrieved concentration from the fit is 4.98(6) ppmv. Figure 5(a) shows the full ro-vibrational band of Methane, while Fig. 5(b) and Fig. 5(c) show enlargements to spectral features in Q and P branches to demonstrate the quality of the measurement and the fitting routine. The residuals are shown in the lower panels. The featureless residuals demonstrate the high precision of the frequency calibration as well as the high quality of the fitting routine. The long-term stability and the linearity of the FTS system, based on the short-wavelength MIR SC source (from NKT), can be found in our previous work [29].

4.2. Long-wavelength supercontinuum source

To demonstrate the performance of the FTS combined with the long-wavelength SC source (from DTU Fotonik), we measured a broadband spectrum of 25.0(7) ppmv of NO diluted in N_2 at atmospheric pressure with 1 GHz spectral resolution, around a center wavelength of 5.25 μm. In this measurement, we changed the balanced detectors to PVI-4TE-10.6 (Vigo Systems) photovoltaic detectors, which are sensitive up to 10.6 μm, but have lower detectivity compare to the PVI-4TE-4 (Vigo Systems) detectors that were used for the short-wavelength SC source. No optical filter was used in this measurement. Note that for all of the measurements using the long-wavelength source, the beam path and the box containing the FTS were purged with nitrogen to minimize the spectral interference by water absorption lines with the measured spectra. The measured spectrum is shown in Fig. 6 (in black, 2000 averages in ~200 minutes) alongside a fitted model of NO spectrum (in red, inverted for clarity) calculated using the HITRAN database parameters and a Voigt profile. The retrieved concentration from the fit is 25.3(6) ppmv. Figure 6(a) shows the full ro-vibrational band of NO, while Fig. 6(b) shows an enlargement to single absorption lines in the R branch, with the residuals in the lower panels.

Optics EXPRESS

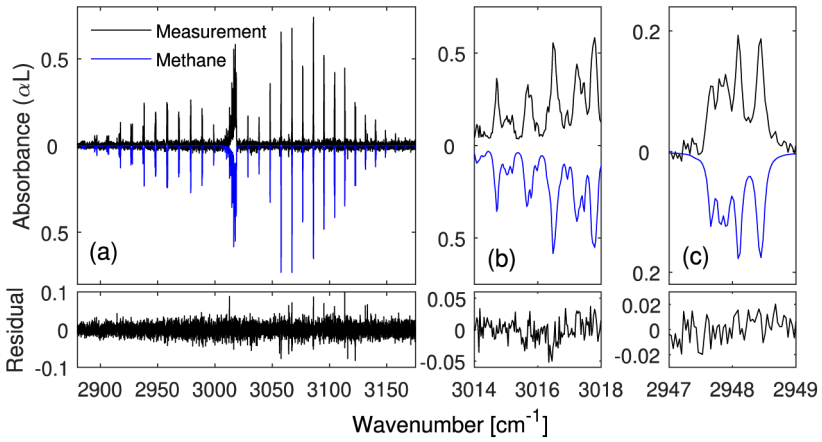

Fig. 5. (a) Measured spectrum (in black, 1 GHz spectral resolution, 250 averages in ~25 minutes) of 5 ppmv of CH_4 diluted in N_2 at 900 mbar total pressure and a fit model spectrum (in blue, inverted) based on the HITRAN database parameters and a Voigt profile. (b) and (c) Enlargements to different parts of the spectrum. The residuals of the fits are shown in the lower panels.

Again, the featureless residuals demonstrate the sufficient precision of the frequency calibration as well as the high quality of the fitting routine.

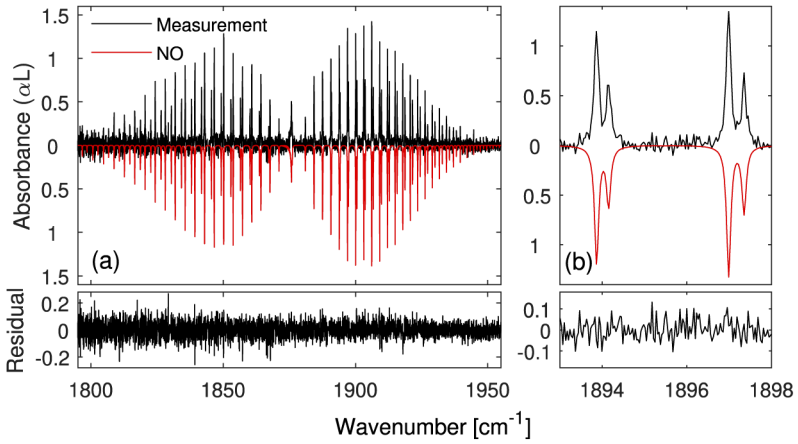

Fig. 6. (a) Measured spectrum (in black, 1 GHz spectral resolution, 2000 averages in ~200 minutes) of 25 ppmv of NO diluted in N_2 at atmospheric pressure and a fit model spectrum (in red, inverted) based on the HITRAN database parameters and a Voigt profile. (b) An enlargement to single absorption lines in the R branch of NO. The residuals of the fits are shown in the lower panels.

Since a long averaging time has been used for the NO measurement, the long-term stability of the FTS needs to be verified. We used the normalized transmission spectra of the NO measurement for different number of averages, ranging from 100 to 2000, and calculated the standard deviation of the noise in the center of the spectrum (away from individual absorption lines) for each averaged spectra. The results are shown in Fig. 7, where the standard deviation of the noise for varying number of averages is depicted (blue circles), alongside a fitted square root of number of averages (red dashed line) indicating the white noise behavior. The standard

Optics EXPRESS

deviation of the noise follows the white noise response for 2000 averages and the residual of the fit for the NO measurement (averaged for 2000 times) is featureless, as shown in Fig. 6. These indicate that the measured intensity and the frequency calibration of the instrument are clearly not affected by the long-term drifts at least up to 2000 averages (~200 minutes).

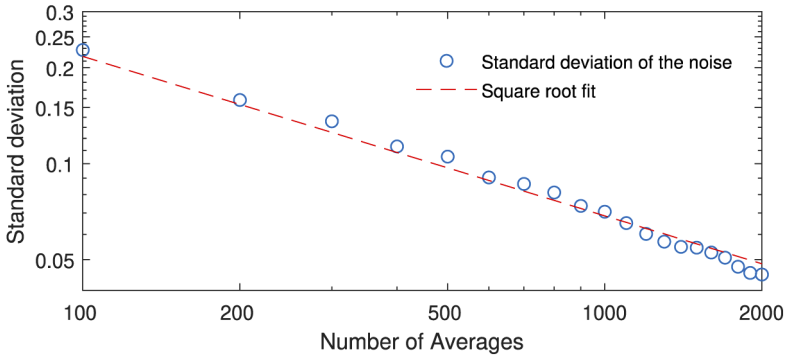

Fig. 7. The standard deviation of the noise on the normalize transmission spectrum for varying number of averages (blue circles) and a fitted square root of number of averages (red dashed line) indicating the white noise behavior.

For longer wavelength operation, we measured the full ro-vibrational band of SO_2, 30.0(9) ppmv diluted in N_2 at atmospheric pressure, around 7.4 μm with 3 GHz spectral resolution. In this measurement, we used PVI-4TE-10.6 (Vigo Systems) photovoltaic detectors and an optical long-pass filter, with a cut-on wavelength of 6.0 μm (Edmund Optics), in the beam path after the MPC. The measured spectrum is shown in Fig. 8 (in black, 4000 averages in ~130 minutes) alongside a fitted model of SO_2 spectrum (in red, inverted for clarity) calculated using the HITRAN database parameters and a Voigt profile. The retrieved concentration from the fit is 29.4(8) ppmv and the residual is shown in the lower panel. The residual from the SO_2 fit is rather featureless. However, there are atmospheric water lines absorbing close to 100% in both the sample and background spectra, despite the nitrogen purging. Due to the very strong absorption and different water concentrations in the sample and background measurements, these water lines remain in the normalized spectrum and consequently in the absorbance spectrum. These water lines cannot be modeled perfectly due to their very strong absorption. We fitted a model of the H_2O spectrum (in blue, inverted for clarity) calculated using the HITRAN database parameters and a Voigt profile alongside the SO_2 model spectra. However, a typical W-shaped residual remains at the position of the water lines. Note that since these water lines are quite scarce in the measured spectrum they do not affect the precision of the SO_2 fit.

4.3. Noise performance and detection limits

To compare the noise performance of the system using the short- and long-wavelength SC sources as well as the two different detector types in the balanced detection scheme, we calculated the standard deviation of the noise on the normalized background spectra of N_2 (both measured with 1 GHz = 0.033 cm^{-1} spectral resolution), where the spectra have their highest SNR (with no optical spectral filters) for the same number of averaged samples (250 in ~25 minutes). Using the short-wavelength SC source and PVI-4TE-4 detectors, this value is $\sigma = 1.2\times10^{-2}$, while for the long-wavelength SC source and PVI-4TE-10.6 detectors, it is $\sigma = 9.0\times10^{-2}$. Therefore the noise of the instrument using the long-wavelength SC source is ~7.5 times larger than the noise using the short-wavelength SC source. This is expected, since the long-wavelength SC source requires a soliton-based spectrum out of the ZBLAN fiber to cascade into the subsequent chalcogenide fibers [30,34,35]. In contrast, the short-wavelength SC source stops at the ZBLAN fiber, whose core

Optics EXPRESS

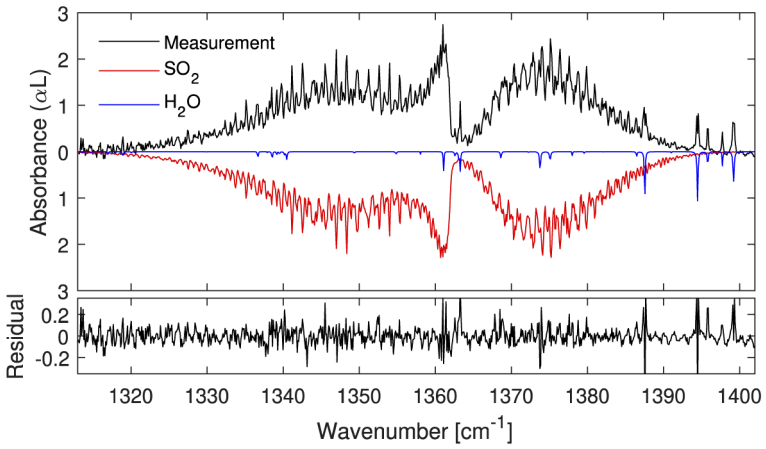

Fig. 8. Measured spectrum (in black, 3 GHz spectral resolution, 4000 averages in ~130 minutes) of 30 ppmv of SO_2 diluted in N_2 at atmospheric pressure and fit model spectra of SO_2 (in red, inverted) and H_2O (in blue, inverted) both based on the HITRAN database parameters and Voigt profiles. The residual of the fit is shown in the lower panel.

diameter can then be chosen for optimum use of dispersive waves and a low-noise performance [35]. Using the retrieved standard deviation of the noise, the Noise Equivalent Absorption Sensitivity (NEAS) per spectral element can be calculated, which is defined as

$$\mathrm{NEAS} = \frac{\sigma\sqrt{2T}}{L\sqrt{M}}, \tag{1}$$

where σ is the standard deviation of the noise in the baseline, L is the interaction path length (31.2 m), T is the measurement time of a single averaged spectrum (25 minutes), and M is the number of spectral elements (1500 cm^{-1} / 0.033 cm^{-1} ≈ 45000 for the short-wavelength SC source and 3000 cm^{-1} / 0.033 cm^{-1} ≈ 90000 for the long-wavelength SC source) [36]. NEAS value is 9.9×10^{-7} cm^{-1} $Hz^{-1/2}$ per spectral element for the short-wavelength SC source and detectors and 5.3×10^{-6} cm^{-1} $Hz^{-1/2}$ per spectral element for the long-wavelength SC source and detectors. Table 1 compares the spectral coverage, spectral resolution and NEAS of the developed spectrometer(s) to the other broadband MIR spectroscopy systems. FTS systems based on the frequency combs, and dual-comb spectroscopy based on nonlinear conversion of NIR femtosecond fiber lasers, provide a better spectral resolution and NEAS; however, they are more complicated, bulky, and expensive. Dual-comb spectrometers based on QCLs usually provide a very narrow bandwidth and a coarse spectral resolution, but in a very small footprint with a robust operation. FTIRs based on thermal sources can provide a rather good NEAS, however usually with a very coarse spectral resolution. Their SNR decreases drastically for high resolution measurements [37].

5. Conclusions and outlook

Novel mid-infrared (MIR) supercontinuum (SC) sources provide broad spectral coverage and high optical power, within a spatially coherent beam. These features are very desirable for multispecies trace gas detection, using a long optical interaction length in a multipass cell and a Fourier transform spectrometer (FTS). We developed a compact and cost-effective FTS, using off-the-shelf components, and verified its operation using two different MIR SC sources covering different wavelength ranges from 1.4 μm to 10.5 μm. For the first time, to the best of our knowledge, we demonstrated trace gas detection with a MIR SC source whose spectral

Optics EXPRESS

range is beyond 5 μm. The ultra-broadband coverage of the instrument is extending deep into the molecular fingerprint region, allowing detection of a considerable number of important gas species. We applied three different detection schemes: using a single detector in baseband, synchronous detection using a lock-in amplifier, and baseband balanced detection. The best results were achieved using the balanced detection. We measured the absorbance spectra of different species, using the short- and the long-wavelength SC sources to demonstrate the total performance of the system. We also compared the performance of the two SC sources in terms of the spectral noise and detection sensitivity. The FTS combined with MIR SC sources is 1–2 orders of magnitude more noisy than a similar FTS system combined with a MIR optical frequency comb. However, the simplicity, compactness, reliability, and lower cost of the MIR SC sources make them a viable alternative for real-life applications. Moreover, the rapid evolution in MIR SC sources promises improved noise features in a near future. An auto-balanced detection scheme would further increase the SNR of the measured spectra, by dynamically and precisely balancing the output of the two photodetectors for the entire range of the optical path difference. The FTS instrument can also be adopted for long-path, free-space multispecies detection, where an ultra-broadband absorption spectrum in the 2–10.5 μm region can be retrieved simultaneously.

Table 1. Comparison of the developed spectrometer(s) to the other broadband MIR spectroscopy systems.

Spectroscopy method	Reference/Note	Spectral coverage (μm)	Spectral resolution (GHz)	NEAS (cm^{-1} $Hz^{-1/2}$ per spec. elem.)
SC-based FTS	This work, Short-wavelength source	2.4–4.1	1	9.9×10^{-7}
	This work, Long wavelength source	2–10.5	1	5.3×10^{-6}
Frequency comb-based FTS	[18], OPO pumped by a fs-fiber laser	3.2–3.5 & 4.8–5.3	0.25[a]	5.7 & 3.1×10^{-8}
Dual-comb spectroscopy	[38], OPOs pumped by fs-fiber lasers	3.1–5.5	0.115[a]	8.5×10^{-9}
	[39,40], DFGs pumped by fs-lasers	2.6–5.2	0.20[a]	$\sim2\times10^{-9}$
	[24], QCL-based frequency combs	8.1–8.6	10[a]	$\sim8\times10^{-7}$
FTIR	[41], Bruker IRcube FTIR	2.5–5	30	$\sim2\times10^{-8}$

[a]No spectral interleaving was considered.

Funding. H2020 Industrial Leadership (101015825, 732968); H2020 Fast Track to Innovation (958840); European Commission (NWE 363); Stichting voor de Technische Wetenschappen (TTW, 14709).

Acknowledgments. The authors also would like to thank Dr. Laurent Balet for the proof reading of the manuscript.

Disclosures. The authors declare no direct financial relationship between the companies manufacturing the SC sources (NKT and NORBLIS) and the academic institute developed the FTS (Radboud University), and that the companies did not directly funded this study/manuscript. The SC sources were developed in the framework of the projects mentioned in the funding section, specifically EU H2020-ICT-29 (FLAIR project, 732968). The development of the FTS instrument and reporting of the results were carried out by the authors at Radboud University, independent of the companies that manufacture the SC sources.

Data availability. Data underlying the results presented in this paper are not publicly available at this time but may be obtained from the authors upon reasonable request.

Optics EXPRESS

References

1. M. Seidel, X. Xiao, S. A. Hussain, G. Arisholm, A. Hartung, K. T. Zawilski, P. G. Schunemann, F. Habel, M. Trubetskov, V. Pervak, O. Pronin, and F. Krausz, "Multi-watt, multi-octave, mid-infrared femtosecond source," Sci. Adv. **4**(4), eaaq1526 (2018).
2. C. R. Petersen, P. M. Moselund, L. Huot, L. Hooper, and O. Bang, "Towards a table-top synchrotron based on supercontinuum generation," Infrared Phys. Technol. **91**, 182–186 (2018).
3. R. A. Martinez, K. W. Guo, T. Q. Zhai, F. L. Terry, L. E. Pierce, M. N. Islam, R. Gibson, J. M. Reed, R. G. Bedford, L. Maksymiuk, M. J. Freeman, B. A. Gorin, N. P. Christian, and A. I. Ifarraguerri, "Active mid-wave to long-wave supercontinuum FTIR sensor for standoff chemical detection," J. Lightwave Technol. **37**(14), 3626–3636 (2019).
4. R. A. Martinez, G. Plant, K. W. Guo, B. Janiszewski, M. J. Freeman, R. L. Maynard, M. N. Islam, F. L. Terry, O. Alvarez, F. Chenard, R. Bedford, R. Gibson, and A. I. Ifarraguerri, "Mid-infrared supercontinuum generation from 1.6 to > 11 μm using concatenated step-index fluoride and chalcogenide fibers," Opt. Lett. **43**(2), 296–299 (2018).
5. S. Venck, F. St-Hilaire, L. Brilland, A. N. Ghosh, R. Chahal, C. Caillaud, M. Meneghetti, J. Troles, F. Joulain, S. Cozic, S. Poulain, G. Huss, M. Rochette, J. M. Dudley, and T. Sylvestre, "2-10 μm mid-infrared fiber-based supercontinuum laser source: experiment and simulation," Laser Photon. Rev. **14**(6), 2000011 (2020).
6. K. Jiao, J. M. Yao, Z. M. Zhao, X. G. Wang, N. Si, X. S. Wang, P. Chen, Z. G. Xue, Y. M. Tian, B. Zhang, P. Q. Zhang, S. X. Dai, Q. H. Nie, and R. P. Wang, "Mid-infrared flattened supercontinuum generation in all-normal dispersion tellurium chalcogenide fiber," Opt. Express **27**(3), 2036–2043 (2019).
7. N. R. Newbury, B. R. Washburn, K. L. Corwin, and R. S. Windeler, "Noise amplification during supercontinuum generation in microstructure fiber," Opt. Lett. **28**(11), 944–946 (2003).
8. U. Moller, S. T. Sorensen, C. Jakobsen, J. Johansen, P. M. Moselund, C. L. Thomsen, and O. Bang, "Power dependence of supercontinuum noise in uniform and tapered PCFs," Opt. Express **20**(3), 2851–2857 (2012).
9. D. S. S. Rao, R. D. Engelsholm, I. B. Gonzalo, B. B. Zhou, P. Bowen, P. M. Moselund, O. Bang, and M. Bache, "Ultra-low-noise supercontinuum generation with a flat near-zero normal dispersion fiber," Opt. Lett. **44**(9), 2216–2219 (2019).
10. K. Kwarkye, M. Jensen, R. D. Engelsholm, M. K. Dasa, D. Jain, P. Bowen, P. M. Moselund, C. R. Petersen, and O. Bang, "In-amplifier and cascaded mid-infrared supercontinuum sources with low noise through gain-induced soliton spectral alignment," Sci. Rep. **10**(1), 8230 (2020).
11. A. B. Seddon, B. Napier, I. Lindsay, S. Lamrini, P. M. Moselund, N. Stone, O. Bang, and M. Farries, "Prospective on using fibre mid-infrared supercontinuum laser sources for in vivo spectral discrimination of disease," Analyst **143**(24), 5874–5887 (2018).
12. F. Borondics, M. Jossent, C. Sandt, L. Lavoute, D. Gaponov, A. Hideur, P. Dumas, and S. Fevrier, "Supercontinuum-based Fourier transform infrared spectromicroscopy," Optica **5**(4), 378–381 (2018).
13. C. R. Petersen, N. Prtljaga, M. Farries, J. Ward, B. Napier, G. R. Lloyd, J. Nallala, N. Stone, and O. Bang, "Mid-infrared multispectral tissue imaging using a chalcogenide fiber supercontinuum source," Opt. Lett. **43**(5), 999–1002 (2018).
14. N. M. Israelsen, C. R. Petersen, A. Barh, D. Jain, M. Jensen, G. Hannesschlager, P. Tidemand-Lichtenberg, C. Pedersen, A. Podoleanu, and O. Bang, "Real-time high-resolution mid-infrared optical coherence tomography," Light: Sci. Appl. **8**(1), 11 (2019).
15. K. E. Jahromi, M. Nematollahi, Q. Pan, M. A. Abbas, S. M. Cristescu, F. J. M. Harren, and A. Khodabakhsh, "Sensitive multi-species trace gas sensor based on a high repetition rate mid-infrared supercontinuum source," Opt. Express **28**(18), 26091–26101 (2020).
16. F. Adler, P. Maslowski, A. Foltynowicz, K. C. Cossel, T. C. Briles, I. Hartl, and J. Ye, "Mid-infrared Fourier transform spectroscopy with a broadband frequency comb," Opt. Express **18**(21), 21861–21872 (2010).
17. S. Meek, A. Poisson, G. Guelachvili, T. W. Hansch, and N. Picque, "Fourier transform spectroscopy around 3 (m with a broad difference frequency comb," Appl. Phys. B **114**(4), 573–578 (2014).
18. A. Khodabakhsh, V. Ramaiah-Badarla, L. Rutkowski, A. C. Johansson, K. F. Lee, J. Jiang, C. Mohr, M. E. Fermann, and A. Foltynowicz, "Fourier transform and Vernier spectroscopy using an optical frequency comb at 3-5.4 μm," Opt. Lett. **41**(11), 2541–2544 (2016).
19. P. Maslowski, K. F. Lee, A. C. Johansson, A. Khodabakhsh, G. Kowzan, L. Rutkowski, A. A. Mills, C. Mohr, J. Jiang, M. E. Fermann, and A. Foltynowicz, "Surpassing the path-limited resolution of Fourier-transform spectrometry with frequency combs," Phys. Rev. A **93**(2), 021802 (2016).
20. A. Foltynowicz, P. Maslowski, A. J. Fleisher, B. J. Bjork, and J. Ye, "Cavity-enhanced optical frequency comb spectroscopy in the mid-infrared application to trace detection of hydrogen peroxide," Appl. Phys. B **110**(2), 163–175 (2013).
21. J. Sotor, T. Martynkien, P. G. Schunemann, P. Mergo, L. Rutkowski, and G. Sobon, "All-fiber mid-infrared source tunable from 6 to 9 μm based on difference frequency generation in OP-GaP crystal," Opt. Express **26**(9), 11756–11763 (2018).
22. Q. Ru, T. Kawamori, P. G. Schunemann, S. Vasilyev, S. B. Mirov, and K. L. Vodopyanov, "Two-octave-wide (3-12 μm) subharmonic produced in a minimally dispersive optical parametric oscillator cavity," Opt. Lett. **46**(4), 709–712 (2021).
23. L. A. Sterczewski, C. Frez, S. Forouhar, D. Burghoff, and M. Bagheri, "Frequency-modulated diode laser frequency combs at 2 μm wavelength," APL Photonics **5**(7), 076111 (2020).

Optics EXPRESS

24. M. Gianella, A. Nataraj, B. Tuzson, P. Jouy, F. Kapsalidis, M. Beck, M. Mangold, A. Hugi, J. Faist, and L. Emmenegger, "High-resolution and gapless dual comb spectroscopy with current-tuned quantum cascade lasers," Opt. Express **28**(5), 6197–6208 (2020).
25. C. A. Michaels, T. Masiello, and P. M. Chu, "Fourier Transform Spectrometry with a Near-Infrared Supercontinuum Source," Appl. Spectrosc. **63**(5), 538–543 (2009).
26. V. V. Goncharov and G. E. Hall, "Supercontinuum Fourier transform spectrometry with balanced detection on a single photodiode," J. Chem. Phys. **145**(8), 084201 (2016).
27. T. Mikkonen, C. Amiot, A. Aalto, K. Patokoski, G. Genty, and J. Toivonen, "Broadband cantilever-enhanced photoacoustic spectroscopy in the mid-IR using a supercontinuum," Opt. Lett. **43**(20), 5094–5097 (2018).
28. I. Zorin, J. Kilgus, K. Duswald, B. Lendl, B. Heise, and M. Brandstetter, "Sensitivity-enhanced Fourier transform mid-infrared spectroscopy using a supercontinuum laser source," Appl. Spectrosc. **74**(4), 485–493 (2020).
29. K. E. Jahromi, M. Nematollahi, R. Krebbers, M. A. Abbas, A. Khodabakhsh, and F. J. M. Harren, "Fourier transform and grating-based spectroscopy with a mid-infrared supercontinuum source for trace gas detection in fruit quality monitoring," Opt. Express **29**(8), 12381–12397 (2021).
30. G. Woyessa, K. Kwarkye, M. K. Dasa, C. R. Petersen, R. Sidharthan, S. Chen, S. Yoo, and O. Bang, "Power stable 1.5–10.5 μm cascaded mid-infrared supercontinuum laser without thulium amplifier," Opt. Lett. **46**(5), 1129–1132 (2021).
31. A. Libert, X. Urbain, B. Fabre, M. Daman, and C. Lauzin, "Design and characteristics of a cavity-enhanced Fourier-transform spectrometer based on a supercontinuum source," Rev. Sci. Instrum. **91**(11), 113104 (2020).
32. T. J. Johnson, R. L. Sams, and S. W. Sharpe, "The PNNL quantitative infrared database for gas-phase sensing: A spectral library for environmental, hazmat and public safety standoff detection," in *Chemical and Biological Point Sensors for Homeland Defense*, A. J. Sedlacek, S. D. Cjristesen, R. Colton, and T. VoDinh, eds. (Spie-Int Soc Optical Engineering, Bellingham, 2004), pp. 159–167.
33. I. E. Gordon, L. S. Rothman, C. Hill, R. V. Kochanov, Y. Tan, P. F. Bernath, M. Birk, V. Boudon, A. Campargue, K. V. Chance, B. J. Drouin, J. M. Flaud, R. R. Gamache, J. T. Hodges, D. Jacquemart, V. I. Perevalov, A. Perrin, K. P. Shine, M. A. H. Smith, J. Tennyson, G. C. Toon, H. Tran, V. G. Tyuterev, A. Barbe, A. G. Csaszar, V. M. Devi, T. Furtenbacher, J. J. Harrison, J. M. Hartmann, A. Jolly, T. J. Johnson, T. Karman, I. Kleiner, A. A. Kyuberis, J. Loos, O. M. Lyulin, S. T. Massie, S. N. Mikhailenko, N. Moazzen-Ahmadi, H. S. P. Muller, O. V. Naumenko, A. V. Nikitin, O. L. Polyansky, M. Rey, M. Rotger, S. W. Sharpe, K. Sung, E. Starikova, S. A. Tashkun, J. Vander Auwera, G. Wagner, J. Wilzewski, P. Wcislo, S. Yu, and E. J. Zak, "The HITRAN2016 molecular spectroscopic database," J. Quant. Spectrosc. Radiat. Transf. **203**, 3–69 (2017).
34. I. Kubat, C. R. Petersen, U. V. Moller, A. Seddon, T. Benson, L. Brilland, D. Mechin, P. M. Moselund, and O. Bang, "Thulium pumped mid-infrared 0.9-9 μm supercontinuum generation in concatenated fluoride and chalcogenide glass fibers," Opt. Express **22**(4), 3959–3967 (2014).
35. C. R. Petersen, P. M. Moselund, C. Petersen, U. Moller, and O. Bang, "Spectral-temporal composition matters when cascading supercontinua into the mid-infrared," Opt. Express **24**(2), 749–758 (2016).
36. N. R. Newbury, I. Coddington, and W. Swann, "Sensitivity of coherent dual-comb spectroscopy," Opt. Express **18**(8), 7929–7945 (2010).
37. D. W. T. Griffith and I. M. Jamie, "Fourier Transform Infrared Spectrometry in Atmospheric and Trace Gas Analysis," in *Encyclopedia of Analytical Chemistry*, R. A. Meyers, ed. (Wiley, 2006).
38. A. V. Muraviev, V. O. Smolski, Z. E. Loparo, and K. L. Vodopyanov, "Massively parallel sensing of trace molecules and their isotopologues with broadband subharmonic mid-infrared frequency combs," Nat. Photonics **12**(4), 209–214 (2018).
39. G. Ycas, F. R. Giorgetta, E. Baumann, I. Coddington, D. Herman, S. A. Diddams, and N. R. Newbury, "High-coherence mid-infrared dual-comb spectroscopy spanning 2.6 to 5.2 μm," Nat. Photonics **12**(4), 202–208 (2018).
40. G. Ycas, F. R. Giorgetta, J. T. Friedlein, D. Herman, K. C. Cossel, E. Baumann, N. R. Newbury, and I. Coddington, "Compact mid-infrared dual-comb spectrometer for outdoor spectroscopy," Opt. Express **28**(10), 14740–14752 (2020).
41. D. W. T. Griffith, N. M. Deutscher, C. Caldow, G. Kettlewell, M. Riggenbach, and S. Hammer, "A Fourier transform infrared trace gas and isotope analyser for atmospheric applications," Atmos. Meas. Tech. **5**(10), 2481–2498 (2012).